# SANDIA REPORT

SAND2004-0152
Unlimited Release
Printed January, 2004

# Monolithic Supports with Unique Geometries and Enhanced Mass Transfer

Robert M. Ferrizz, John N. Stuecker, Joseph Cesarano III, and James E. Miller

Prepared by
Sandia National Laboratories
Albuquerque, New Mexico 87185 and Livermore, California 94550

Sandia is a multiprogram laboratory operated by Sandia Corporation,
a Lockheed Martin Company, for the United States Department of Energy's
National Nuclear Security Administration under Contract DE-AC04-94AL85000.



Issued by Sandia National Laboratories, operated for the United States Department of Energy by Sandia Corporation.



Available to DOE and DOE contractors from
U.S. Department of Energy
Office of Scientific and Technical Information
P.O. Box 62
Oak Ridge, TN 37831

Telephone: (865)576-8401
Facsimile: (865)576-5728
E-Mail: reports@adonis.osti.gov
Online ordering: http://www.doe.gov/bridge

Available to the public from
U.S. Department of Commerce
National Technical Information Service
5285 Port Royal Rd
Springfield, VA 22161

Telephone: (800)553-6847
Facsimile: (703)605-6900
E-Mail: orders@ntis.fedworld.gov
Online order: http://www.ntis.gov/help/ordermethods.asp?loc=7-4-0#online

**SAND2004-0152**
Unlimited Release
Printed January, 2004

# Monolithic Supports with Unique Geometries and Enhanced Mass Transfer

Robert M. Ferrizz, John N. Stuecker[#], Joseph Cesarano III[#], and James E. Miller

Chemical Synthesis and Nanomaterials Department
[#]Ceramic Materials Department
Sandia National Laboratories
P.O. Box 5800
Albuquerque, NM 87185-1349

## Abstract

*The catalytic combustion of natural gas has been the topic of much research over the past decade. Interest in this technology results from a desire to decrease or eliminate the emissions of harmful nitrogen oxides ($NO_X$) from gas turbine power plants. A low-pressure drop catalyst support, such as a ceramic monolith, is ideal for this high-temperature, high-flow application. A drawback to the traditional honeycomb monoliths under these operating conditions is poor mass transfer to the catalyst surface in the straight-through channels. "Robocasting" is a unique process developed at Sandia National Laboratories that can be used to manufacture ceramic monoliths with alternative 3-dimensional geometries, providing tortuous pathways to increase mass transfer while maintaining low pressure drops.*

*This report details the mass transfer effects for novel 3-dimensional robocast monoliths, traditional honeycomb-type monoliths, and ceramic foams. The mass transfer limit is experimentally determined using the probe reaction of CO oxidation over a Pt / $\gamma$-$Al_2O_3$ catalyst, and the pressure drop is measured for each monolith sample. Conversion versus temperature data is analyzed quantitatively using well-known dimensionless mass transfer parameters. The results show that, relative to the honeycomb monolith support, considerable improvement in mass transfer efficiency is observed for robocast samples synthesized using an FCC-like geometry of alternating rods. Also, there is clearly a trade-off between enhanced mass transfer and increased pressure drop, which can be optimized depending on the particular demands of a given application.*

## Acknowledgements

The authors would like to thank Lindsey Evans and Ronald Sandoval for their general help and guidance with the flow reactor system and chemical synthesis procedures, and Paul Dailey for performing the pressure drop measurements. This work was supported through Sandia's laboratory directed research and development (LDRD) program.

# Contents


1. Introduction ..... 7
2. Theory: Quantifying Mass Transfer ..... 7
   - 2.1 Kinetic Regimes ..... 7
   - 2.2 Mass Transfer Control ..... 9
   - 2.3 Sherwood Number ..... 10
   - 2.4 $J_D$ Factor ..... 11
3. Experimental ..... 12
   - 3.1 Monolith Supports ..... 12
   - 2.2 Washcoating ..... 13
   - 3.3 Activity Measurements ..... 14
   - 3.4 Pressure Drop Measurements ..... 15
4. Results ..... 15
   - 4.1 Honeycomb Monoliths ..... 15
   - 4.2 Robocast Monoliths (FCC and SC) ..... 18
   - 4.3 Robocast Monolith (FCC-74) and Ceramic Foams ..... 22
   - 4.4 Quantitative Analysis – Sherwood Number ..... 25
   - 4.5 Quantitative Analysis – $J_D$ Factor ..... 26
   - 4.5 Additional Comments ..... 28
5. Conclusions ..... 29

References ..... 30


# Figures


1. Idealized plot of reaction rate versus temperature ..... 8
2. Schematic representations of the FCC, SC, and FCC-74 geometries ..... 13
3. CO conversion for a Pt/$\gamma$-$Al_2O_3$-coated honeycomb monolith ..... 16
4. Actual and kinetically-limited CO conversion over the honeycomb sample ..... 17
5. Arrhenius plot for the 13,000 sccm honeycomb monolith data ..... 17
6. Plot of $k_{APP}$ vs. $T^{3/2}$ for the 13,000 sccm honeycomb monolith data ..... 18
7. CO conversion (500 sccm) for the Robo FCC, Robo SC, and honeycomb samples ..... 19
8. CO conversion (10,000 sccm) for the Robo FCC, Robo SC, and honeycomb samples ..... 20
9. CO conversion (13,000 sccm) for the Robo FCC, Robo SC, and honeycomb samples ..... 21
10. Pressure Drop for the Robo FCC, Robo SC, and honeycomb samples ..... 21
11. Pressure Drop for the Robo FCC-74, ceramic foam, and honeycomb samples ..... 23
12. CO conversion (10,000 sccm) for all samples ..... 24
13. CO conversion (13,000 sccm) for all samples ..... 24
14. $N_{SH}$ vs. $N_{GZ}$ for all samples & empirical correlations ..... 25
15. $\varepsilon J_D$ vs. $N_{RE}$ for all samples & empirical correlations ..... 27


# Tables


1. Physical properties of honeycomb, robocast, and foam monolith samples ..... 13
2. Catalyst loadings for the honeycomb, robocast, and foam monolith samples ..... 14

# Nomenclature

| | |
|---|---|
| A | Arrhenius pre-exponential factor ($s^{-1}$) |
| C | reactant concentration (mol $m^{-3}$) |
| CI | concentration at reactor inlet (mol $m^{-3}$) |
| CO | concentration at reactor outlet (mol $m^{-3}$) |
| CP | heat capacity (J $kg^{-1}$ $K^{-1}$) |
| CSA | cross-sectional area ($m^2$) |
| d | monolith diameter (m) |
| D | diffusivity ($m^2$ $s^{-1}$) |
| $d_H$ | hydraulic diameter (m) |
| $E_{ACT}$ | activation energy (kJ $mol^{-1}$) |
| G | mass velocity (kg $s^{-1}$ $m^{-2}$) |
| h | heat transfer coefficient (W $m^{-2}$ $K^{-1}$) |
| $J_D$ | dimensionless mass transfer factor |
| $k_{APP}$ | experimentally observed rate constant ($s^{-1}$) |
| $k_{HOMO}$ | rate constant for homogeneous reaction ($s^{-1}$) |
| $k_{KIN}$ | first order kinetic rate constant ($s^{-1}$) |
| $k_{MT}$ | mass transfer coefficient (m $s^{-1}$) |
| L | monolith length (m) |
| $N_{GZ}$ | Graetz number |
| $N_{PR}$ | Prandtl number |
| $N_{RE}$ | Reynolds number |
| $N_{SC}$ | Schmidt number |
| $N_{SH}$ | Sherwood number |
| P | pressure (Pa) |
| r | reaction rate, (monolith) volume basis (mol $m^{-3}$ $s^{-1}$) |
| R | gas constant (8.314 J $mol^{-1}$ $K^{-1}$) |
| S | geometric surface area (extrinsic surface area per volume monolith) ($m^2$ $m^{-3}$) |
| SV | space velocity (flow rate per monolith volume) ($s^{-1}$) |
| T | temperature (K) |
| V | volumetric flow rate ($m^3$ $s^{-1}$) |
| $V_{MONO}$ | monolith volume ($m^3$) |
| X | reactant conversion |
| z | length (m) |
| | |
| $\varepsilon$ | porosity |
| $\eta$ | effectiveness factor |
| $\mu$ | viscosity (kg $m^{-1}$ $s^{-1}$) |
| $\nu$ | velocity (m/s) |
| $\rho$ | density (kg $m^{-3}$) |
| $\tau$ | residence time (s) |

# 1. Introduction

Monolithic reactors, widely utilized for environmental applications (automotive and stationary emissions control), are currently being considered for a large array of additional catalytic applications[1,2]. Monoliths offer several advantages over traditional packed bed systems, perhaps the most significant of these being a high surface to volume ratio, similar to that of very small particles, but with significantly lower pressure drops. This feat is possible due to the large bulk porosity afforded by the monolithic structure, and hence the low resistance to fluid flow.

An inherent weakness of monoliths (as well as other catalyst support systems) is the onset of bulk gas-solid mass transfer limitations[1,3,4]. The standard honeycomb structure of adjacent straight-through channels usually results in a laminar flow pattern in each individual channel. For very active catalysts (or high loadings and high temperature), the rate-limiting step for catalytic reaction can become diffusion of reactants from the gas phase to the catalyst surface. The conditions encountered in catalytic combustion can certainly fall within these criteria. Catalyst supports with 3-dimensional geometric complexity, such as ceramic foams[5,6], can help overcome this effect by providing a more tortuous pathway for fluid flow, introducing turbulence and therefore convective mass and heat transfer.

A potential application of monolithic reactors that has generated considerable interest is that of catalytic combustion[3,4,7-10]. The goal of this process is to stabilize the combustion of very lean natural gas mixtures, reducing the adiabatic temperature rise to less than 1300°C, and therefore significantly reducing or even eliminating the production of harmful $NO_X$ compounds. This demanding application requires a very active catalyst, high mass transfer rates, very high gas flow rates (with space velocities up to $10^6$ $hr^{-1}$), and an exceptionally thermally-stable catalyst. In this paper, experimental results are presented which demonstrate the feasibility of producing unique, customizable, durable monolithic supports that enhance mass transfer through the use of complex, periodic geometries.

# 2. Theory: Quantifying Mass Transfer

## 2.1 Kinetic Regimes

Similar to the porous catalyst pellet of a packed bed, there is a spectrum of kinetic regimes for monolith reactors. Surface kinetics, pore diffusion, gas-solid mass transfer, or even homogeneous reaction may control the rate of reaction. A popular representation[1,3,4,11] of these effects is shown in Figure 1, which plots the reaction rate (i.e. conversion) for a typical reaction in a catalytic monolith versus temperature. Initially, at low temperatures, the reaction rate is controlled by surface kinetics. Equation (1), the Arrhenius equation, illustrates how the kinetic rate constant increases exponentially with temperature.

$$k_{KIN} = A \times \exp\left(-E_{ACT} / R \times T\right) \qquad (1)$$

A point can be reached for which surface kinetics (which may be adjusted for pore diffusion using an effectiveness factor approach[12-14]) exceeds the rate for bulk mass transfer, causing the overall reaction rate to become mass transfer limited. In this regime, transfer of reactants from the fluid flow to the catalytic surface is the rate-limiting step.

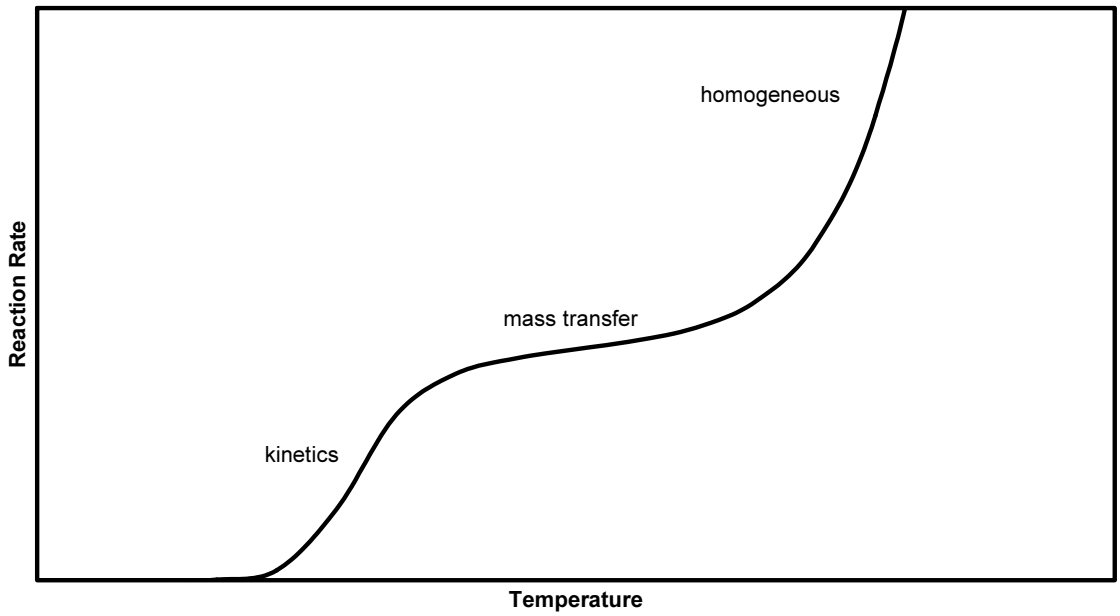


**Figure 1**: Idealized plot of reaction rate (conversion) versus temperature exhibiting the typical rate-controlling regimes for monolith reactors.

The reactant molecules must diffuse through the boundary layer at the gas-solid interface to reach the catalyst, with diffusion rates varying roughly as $T^{3/2}$.

$$k_{MT} = BT^{3/2} \qquad (2)$$

As the mass transfer coefficient (i.e. diffusion rate) increases relatively slowly with temperature, an apparent "plateau" in reaction rate, and thus conversion, is observed during bulk mass transfer control. Finally, homogeneous reaction, with its relatively large activation energy, becomes favorable at high temperatures, at which point the reaction rate soars and conversion rapidly increases to 100%. Using a series/parallel approach, the rate equation for an isothermal, 1st order reaction can be written as follows:

$$-r = \nu \, dC/dz = - k_{APP} \, C; \qquad (3)$$

$$\text{where } k_{APP} = 1 / (1 / S \times k_{MT} + 1 / \eta \times k_{KIN}) + k_{HOMO} \qquad (4)$$

When $\eta \times k_{KIN} > S \times k_{MT}$ (and $k_{HOMO} \sim 0$), the reaction is mass transfer limited. So, when operating strictly in the mass transfer-limited regime (a first order process), the rate equation simplifies to the following:

$$\nu \, dC/dz = - S \, k_{MT} \, C \qquad (5)$$

It is well known[1,6,12,15] that this expression can be simplified to the following:

$$\ln (C_O/C_I) = \ln (1-X) = - S \, k_{MT} \, \tau = - S \, k_{MT} / SV \qquad (6)$$

Therefore, the mass transfer coefficient, $k_{MT}(T)$, can be determined experimentally by obtaining temperature/conversion data at a given flow rate for monolith samples of known geometric properties. Note that space velocity (SV) is defined as the volumetric flow rate per "volume catalyst". In the case of monoliths, the "volume catalyst" is simply the monolith volume (including void space), which can be calculated from the overall monolith dimensions as follows:

$$V_{MONO} = \pi d^2 L / 4 \qquad (7)$$

Using equation (6) to solve for $k_{MT}$ assumes that the reaction is indeed controlled solely by bulk mass transfer[1,15]. Given that there will be a transition region where both reaction kinetics and mass transfer are important, a more precise method for determining $k_{MT}$ from experimental data is the following equation, used in conjunction with equation (4):

$$\ln (1-X) = - k_{APP} / SV \qquad (8)$$

This assumes that an accurate value for $\eta \times k_{KIN}(T)$ is known and that the homogeneous reaction is insignificant. Alternatively, $k_{APP}(T)$ can be experimentally determined using (8), and then equations (1), (2), and (4) can be applied to solve simultaneously for $k_{KIN}$ and $k_{MT}$[6].

## 2.2 Mass Transfer Control

Favorable experimental conditions for operating in the mass transfer-controlled regime include high temperatures and an extremely active catalyst[1]. In addition, a short residence time is required to limit conversion. Experimentally, this is achieved through the use of high flow rates coupled with small monolith dimensions. In this paper, CO oxidation over a $Pt/\gamma\text{-}Al_2O_3$ catalyst is used as the probe reaction for observing mass transfer in monolith samples. Under the correct (and readily attainable) experimental conditions, this reaction is sufficiently active (i.e. the kinetic rate constant is large enough) for inducing mass transfer limitations.

To ensure that the experimental results are, in fact, mass transfer-limited, several data analysis "tools" can be employed. First, visual inspection of the X-T curve can qualitatively reveal whether the curve-shape resembles the idealized version presented in Figure 1. Quantitatively, the activation energy can be calculated based on the observed rate constant (assuming first order kinetics) using an Arrhenius plot of 1/T vs. ln ($k_{APP}$). If the calculated value is relatively large (~125 kJ/mol for CO oxidation over Pt[6,16,17]), then the reaction is kinetically controlled. If the activation energy is relatively small (~10 kJ/mol or less[11]), then the reaction is likely controlled by bulk mass transfer. Furthermore, if $k_{KIN}(T)$ is known, then the experimental data can be plotted versus a "theoretical" kinetically-controlled X-T curve, and large deviations between theory and experiment can be assigned to mass transfer, using the formula for $k_{APP}$ given above. Finally, it is well known[6,11,18] that $k_{MT}$ scales roughly with $T^{3/2}$, as shown in equation (2). Therefore, a plot of $k_{APP}$ vs. $T^{3/2}$ should be approximately linear if mass transfer is controlling the reaction rate.

## 2.3 Sherwood Number

A predominant method to quantify mass transfer found in the literature[1,11,12,14,15,18-21] is the use of the Sherwood number, $N_{SH}$. The Sherwood number is defined as:

$$N_{SH} = k_{MT} \times d_H / D \qquad (9)$$

$N_{SH}$ can be thought of as a dimensionless concentration gradient[22]. In order to calculate the Sherwood number, $k_{MT}(T)$ must first be determined from experimental X-T data, as detailed above. Diffusivity is dependent on system temperature, pressure, and the particular gas phase molecules involved. For CO in air, the following empirical correlation (calculated from Fuller, et al.[23]) has been reported[24]:

$$D = 9.2635 \times 10^{-5} \, T^{1.75} / P \qquad (10)$$

The hydraulic (characteristic) diameter, $d_H$, is another parameter necessary for determining $N_{SH}$. This variable is dependent solely on the physical dimensions and geometry that best characterizes the system in question. For packed beds, the hydraulic diameter is defined as the pellet diameter; for flow in pipes, $d_H$ is the tube diameter. For straight-channel monoliths, $d_H$ is the diameter of an individual channel. However, for ceramic foams and the robocast samples in this study, the channel diameter (or average pore size) is somewhat an abstract quantity. A common expression[6,15,21,25] for determining $d_H$ for unusual geometries is the following:

$$d_H = 4\varepsilon / S \qquad (11)$$

For simple geometries, this expression reduces to 4× the cross-sectional area per wetted perimeter, which in turn reduces to the channel diameter. This expression is often used to calculate the geometric surface area after obtaining microscopy measurements for the channel diameter (or mean pore size). However, for the case of the robocast samples, the geometric surface area is a known quantity (calculated from rod length, diameter, number, and monolith dimensions), while $d_H$ is difficult to precisely measure. Therefore, for the robocast samples, bulk porosity and geometric surface area are used to solve for $d_H$.

There are many empirical correlations derived for many different catalytic systems that relate the Sherwood number to other system parameters, such as fluid velocity, viscosity, density, etc. These correlations are often presented in the form of $N_{SH}$ as a function of the Reynolds and Schmidt numbers. Several relations have been reported in the literature that specifically address mass transfer for honeycomb monoliths.

Uberoi and Pereira[12] proposed the following model for mass transfer in square monolith channels, based on experimental CO oxidation results (using a similar approach to the one detailed in this report):

$$N_{SH} = 2.696 \left(1 + 0.139 \, N_{SC} \, N_{RE} \, (d_H / L)\right)^{0.81} \qquad (12)$$

Note that the Reynolds and Schmidt numbers are defined as follows:

$$N_{RE} = \nu \rho d_H / \mu \qquad (13)$$

$$N_{SC} = \mu / \rho D \qquad (14)$$

Parameters such as viscosity ($\mu$) and density ($\rho$) can be obtained from the Handbook of Chemistry and Physics[26]. Alternatively, density can be calculated from the ideal gas law. The velocity is calculated from the flow rate, porosity, and cross-sectional area as follows[1]:

$$\nu = V / (CSA \times \varepsilon) \qquad (15)$$

Hawthorn[19] derived the following semi-analytical expression (using the analytical solution for fully developed laminar flow and limited experimental data) for laminar flow in a monolith channel with developing boundary layers:

$$N_{SH} = B (1 + C (d_H/L) N_{RE} N_{SC})^{0.45} \qquad (16)$$

B and C are parameters dependent on channel geometry and surface roughness, respectively. B is estimated to be 2.976 for square channel monoliths, while C ranges from 0.078 to 0.095 depending on the degree of surface roughness.

Holmgren and Andersson[15] used CO oxidation measurements and CFD simulations to obtain the following expression for gas-solid mass transfer in square channels with rounded corners:

$$N_{SH} = 3.53 \exp (0.0298 N_{RE} (d_H/L) N_{SC}) \qquad (17)$$

The correlations summarized above are often plotted as the Sherwood number versus the Graetz number, where $N_{GZ}$ combines the Reynolds and Schmidt numbers as follows:

$$N_{GZ} = N_{RE} \times (d_H/L) \times N_{SC} \qquad (18)$$

All three of these expressions yield similar plots, and serve as a good starting point for understanding and quantifying the mass transfer enhancements generated by monoliths with unique geometries.

## 2.4 $J_D$ factor

An alternate (but fundamentally similar) method for quantifying mass transfer is through $J_D$, a dimensionless mass transfer factor. $J_D$ is defined as the following[18]:

$$J_D = (k_{MT} / \nu) \times N_{SC}^{2/3} \qquad (19)$$

This empirical correlation is derived from experimental data for laminar and turbulent flow for both gases and liquids. (It is also the exact solution for laminar flow over a flat plate.) Equation (19) is often used in the following equivalent form:

$$J_D = N_{SH} / (N_{RE} \times N_{SC}^{1/3}) \qquad (20)$$

The use of $J_D$ factors is well-established[6,18,25,27,28] for characterizing bulk mass transfer in packed beds. Many empirical expressions relating $J_D$ to the Reynolds number have been developed, and most are of the form shown below:

$$\varepsilon J_D = A N_{RE}^{B} \qquad (21)$$

Two popular correlations are those published by Satterfield[27] (A = 0.487; B = -0.36) and Dwivedi and Upadhyay[28] (A = 0.455; B = -0.407). As these empirical relationships are essentially derived from a packed bed of spheres, where the void space is <50% and the path for fluid flow is extremely tortuous, it is expected that these correlations will serve as an upper limit to the bulk mass transfer efficiency achievable in catalytic monoliths. Recall that the benefit of monoliths versus packed beds is the improved pressure drop, whereas the benefit of unique 3-D monoliths versus traditional honeycomb monoliths is expected to be the enhanced mass transfer.

# 3. Experimental

## 3.1 Monolith Supports

An extruded, honeycomb monolith (square channels, 400 cpsi) was obtained courtesy of Johnson Matthey. Physical properties of this sample are detailed in Table 1, and were obtained from Corning. From this source, smaller samples were prepared, consisting of 52 channels arranged in a cylindrical shape. Ceramic foam samples (20 PPI) were obtained from Selee Corporation. Physical properties of the 20 PPI ceramic foams are also shown in Table 1. Values for the geometric surface area and bulk porosity were obtained from literature sources. In the absence of specific data from Selee, it is assumed that the 20 PPI foams studied in this work are comparable to other 20 PPI foams of known geometric properties[25].

Robocasting is a novel, rapid-prototyping process developed at Sandia National Laboratories that can fabricate structures with controlled geometries from ceramics, polymers, metals, and combinations of these three. For this study, robocast monoliths were constructed by "drawing" a series of interconnected rods in 3 dimensions. The robocast part is designed using CAD software, and the robocasting apparatus then manufactures the part as specified. This process has been described in detail elsewhere[29-32]. Three differently structured robocast samples were used during this study: the first robocast monolith possesses a face-centered cubic (FCC) geometry, the second has a simple cubic (SC) structure, and the third sample is designed with a "modified" FCC structure that possesses a bulk porosity similar to that of an extruded honeycomb. The physical properties of these robocast samples are outlined in Table 1, while schematic representations of these samples are presented in Figure 2. Note that the modified FCC sample uses the same structural template as the FCC monolith, but the rod size is smaller, and every other rod has been removed.

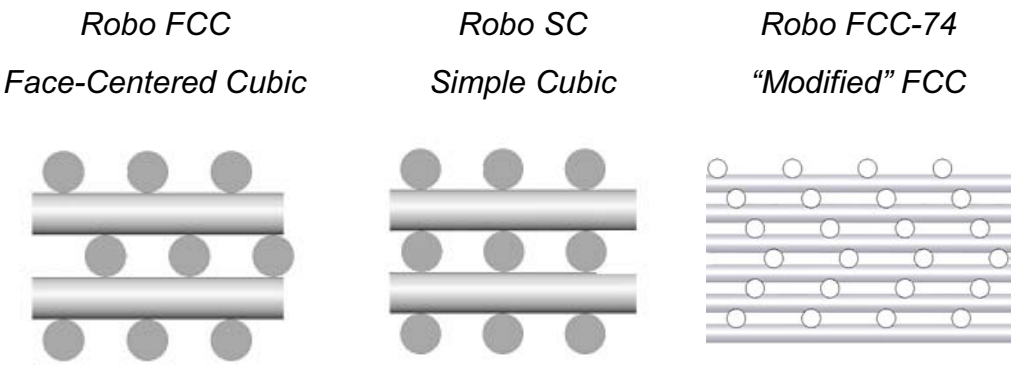


**Figure 2**: Schematic representations of the FCC, SC, and FCC-74 geometries.

The robocast samples were designed to closely mimic a number of different physical properties of the honeycomb samples, most notably the surface-to-volume ratio. In this way, mass transfer effects attributed to differences in geometry (straight channel vs. FCC vs. SC) can be isolated. It should be pointed out that, due to the flexibility of the robocasting process, many other geometries are achievable. Furthermore, the porosity of the rods, which was set at 33% for this study (to match that of cordierite) is variable, as well as the actual material of construction. For example, rather than $Al_2O_3$, it is possible to manufacture a robocast catalyst support composed entirely of the catalytic material, and indeed a barium manganese hexaaluminate ($BaMn_2Al_{10}O_{19}$) monolith that exhibits enhanced catalytic activity for methane combustion has already been synthesized[29].

**Table 1**: physical properties of honeycomb, robocast and foam monolith samples

| | Honeycomb | Robocast FCC & SC | Robocast FCC-74 | Ceramic Foam |
|---|---|---|---|---|
| Material (Primary Phase) | Cordierite ($2\ MgO - 2\ Al_2O_3 - 5\ SiO_2$) | $Al_2O_3$ | $Al_2O_3$ | $Al_2O_3$ |
| Geometry | square channels, 400 cpsi (20 PPI) | FCC or SC | FCC-like | 20 PPI |
| Length | 10.7 mm | 10.5 mm | 10.1 mm | 12.2 mm |
| Diameter | 11.8 mm | 10.7 mm | 10.5 mm | 11.7 mm |
| Geometric Surface Area | 24.5 $cm^2/cm^3$ | 24.2 $cm^2/cm^3$ | 22.5 $cm^2/cm^3$ | 36 $cm^2/cm^3$ |
| Wall Porosity | 33% | 33% | 33% | 0% |
| Bulk Porosity | 74% | 43% | 74% | 85% |

## 3.2 Washcoating

A $\gamma$-$Al_2O_3$ washcoat was applied to the robocast, honeycomb, and foam samples using a procedure similar to that detailed by Toracrona, et al[33]. The washcoat slurry (18 to 35 wt% solids) was prepared by mixing the "solids" (25 wt% boehmite (dispersal, Condea); balance $\gamma$-$Al_2O_3$ (Condea)) with the appropriate weight of deionized water. Darvan 821A (2 wt% based on solids) and methocel (6 wt% based on solids) were also added to enhance dispersion. An $HNO_3$ solution (1.0 N) was then added to the slurry until a pH of 4.0 was attained. The monolith

sample was then immersed in the well-dispersed washcoat slurry for approximately 10 seconds. After waiting an additional 30 seconds, excess slurry was removed by gently blowing air through the monolith. The samples were then dried and calcined (600ºC/2 hours) in air. Finally, a strong air flow was blown through the monolith to remove any poorly adhered $\gamma$-$Al_2O_3$. This procedure was repeated as necessary to acquire the desired washcoat loading. Loadings were determined by weight difference.

The monolith samples were impregnated with Pt by washing with a chloroplatinic acid ($H_2PtCl_6$) solution. Prior to applying this $H_2PtCl_6$ solution, the samples were dipped in deionized $H_2O$ and blown with air, in order to minimize the deposition of Pt in difficult to access interior portions of the monolith walls. The samples were dried and calcined (600ºC/2 hours), and the process repeated until the desired weight loading of Pt was achieved, as determined by weight difference. Additionally, the samples were calcined at 500ºC in an $H_2$/Argon environment to ensure complete reduction to Pt metal. Washcoat weight loadings for $\gamma$-$Al_2O_3$ and Pt for the samples studied in this paper are shown in Table 2. Similar weight loading (~ 3 wt% Pt relative to the cordierite sample) were utilized for each sample.

**Table 2**: catalyst loadings (mg) for the honeycomb, robocast and foam samples

| | Honeycomb | Robo SC | Robo FCC | Robo FCC-74 | Foam |
|---|---|---|---|---|---|
| $\gamma$-$Al_2O_3$ | 72 | 69 | 69 | 58 | 62 |
| Pt | 14 | 14 | 15 | 12 | 15 |

### 3.3 Activity Measurements

Experimental conversion versus temperature data was measured in a flow reactor. This system consisted of a quartz tube and furnace (the reactor), and mass flow controllers to adjust the reactant gas concentration and flowrate. Monolith samples were suspended tightly in the quartz tube using quartz fibers wrapped around the sample exterior. Downstream, a gas chromatograph (poroplot Q and molecular sieve columns) was utilized to measure gas composition exiting the reactor. Two thermocouples were placed inside the quartz tube, and in contact with the monolithic sample; one above and one below (to measure the inlet and outlet gas temperatures). A weighted average[15] ($T_{CALC}$ = 1/3 $T_{IN}$ + 2/3 $T_{OUT}$) was used for all figures and calculations presented in this work.

The oxidation of CO over Pt was used as a probe reaction for mass transfer limitations, due to its high reaction rate. Also, very high gas flowrates (10,000 and 13,000 sccm) were employed to ensure operation in the mass transfer limited regime. The CO oxidation data presented in this work were experimentally obtained using a large excess of oxygen (1% CO in air). Therefore, 1st order kinetic expressions are utilized for the presented quantitative analysis. This assumption is common practice[6,13,15,21] when studying CO oxidation in a highly oxidizing environment, as the inhibitory effect of adsorbed CO on $O_2$ adsorption is mitigated in a large excess of $O_2$.

It is assumed that the effectiveness factor for pore diffusion is the same for each sample, and that this factor is incorporated in the experimentally determined kinetic rate constant. In practical terms, this factor is assumed to be equal to one for all kinetic calculations. This assumption is reasonable, due to the small relative thickness of the washcoat layer, and has precedence in the literature[6,12,15,21,34].

A pressure gauge placed above the reactor was used to measure the pressure of the gas stream. Traditionally, a flow reactor system is operated at atmospheric pressure. However, the very high flowrates utilized, coupled with the significant length of stainless steel tubing, filters, fittings, etc. needed to get the exhaust stream to the GC, created a reactor pressure 6 to 8 psi above that of atmospheric pressure (which is typically only 0.83 atm in Albuquerque, NM).

### 3.4 Pressure Drop Measurements

Pressure drop across the monolith samples was measured in a separate flow system equipped with a differential capacitance manometer (MKS) and readout. Each monolith sample (without washcoat) was suspended in a quartz tube and tested for a wide range of air flowrates (3000 to 11,000 sccm). Pressure drop results for a blank tube were also obtained, in order to correct the monolith results for the "background" pressure losses. Results are presented in the form of pressure drop per unit length (of monolith) versus space velocity.

## 4. Results

### 4.1 Honeycomb Monoliths

The traditional cordierite honeycomb monolith provides a baseline case. Characteristics of this sample are summarized above in the experimental section. The results for CO oxidation are shown in Figure 3. Curve (a) was obtained for a 1% CO in air mixture at a flow rate of 500 sccm (SV ~ 30,000 $hr^{-1}$). 10% CO conversion is observed at 145 °C, with complete conversion occurring shortly thereafter. Even with the large excess of $O_2$, this curve seems to exhibit inverse first order kinetics[13], as conversion increases very sharply to completion above 50%. However, it is possible that the curve is so steep that the small temperature interval between data points was still too large to observe the regular sigmoid shape (i.e. "tailing" at high conversions) that generally accompanies 1st order kinetics[13]. As noted earlier, the 500 sccm CO oxidation results are assumed to be 1st order and free of mass transfer effects. This assumption does not introduce significant error in the calculations that follow for quantifying mass transfer.

The same honeycomb monolith sample was then exposed to a 10,000 sccm flow (SV ~ 575,000 $hr^{-1}$) of 1% CO in air, and the results are presented as curve (b) in Figure 3. As expected, CO light-off has shifted to higher temperatures, with 10% CO conversion now observed at roughly 205 °C. Note, however, that 100% conversion is not rapidly achieved. Rather, at 270°C and 80% CO conversion, the curve quickly levels off, and only small gains in conversion are observed for relatively large increases in temperature. As detailed in Figure 1, this flattening of the X-T curve is classic behavior for a shift in rate-limiting step from surface kinetics to bulk mass transfer control. At 13,000 sccm (SV ~ 750,000 $hr^{-1}$) (Figure 3, curve (c)), the same trend is observed, but the mass transfer "plateau" is now observed at approximately 70% CO conversion. As shown below, the 13,000 sccm data was analyzed quantitatively to conclusively demonstrate that mass transfer control has been achieved at the higher temperatures corresponding to the plateau in conversion. The following analysis was also applied to the other samples and flow rates studied in this work to verify mass transfer control.

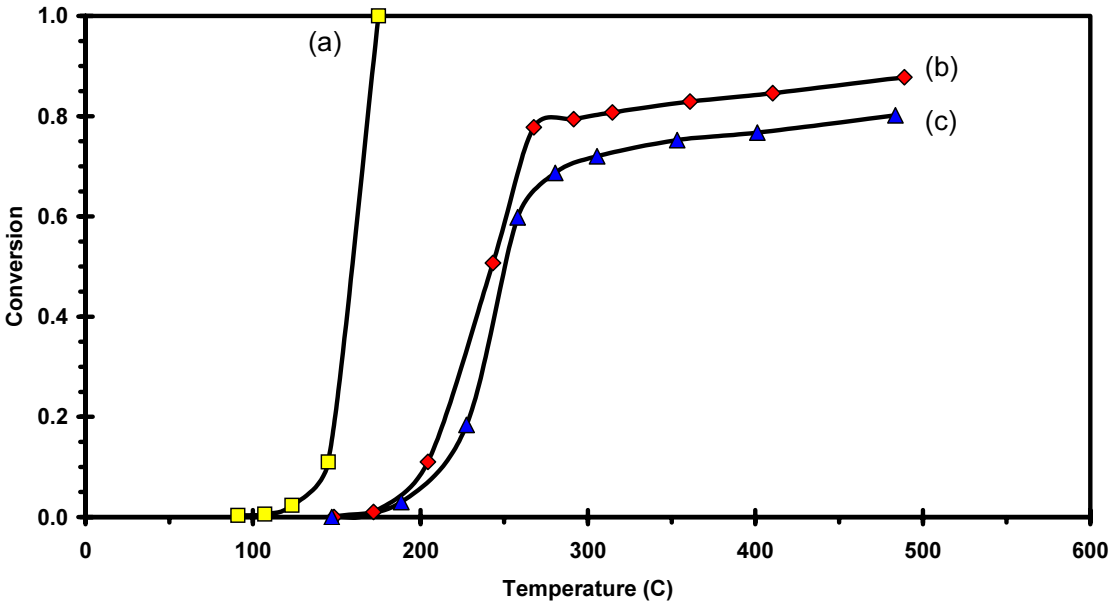


**Figure 3**: CO conversion for a Pt/γ-$Al_2O_3$-coated honeycomb monolith exposed to flows (1% CO in air) of (a) 500 sccm, (b) 10,000 sccm, and (c) 13,000 sccm.

First, assuming 1st order kinetics, the apparent rate constant ($k_{APP}$) was determined from the experimental results for both the 500 and 13,000 sccm flows using equation (8). It is then assumed that $k_{APP} = k_{KIN}$ for the 500 sccm data. A plot of $\ln(k_{KIN})$ vs. 1/T (for the 500 sccm data) yields the following relation (from the Arrhenius equation):

$$\ln(k_{KIN}) = -12941 / T + 31.214 \qquad (22)$$

An activation energy for CO oxidation of 107.6 kJ/mol is calculated from this expression, a value in close agreement with published values in the literature[6,16,17]. Using this expression for $k_{KIN}(T)$, a theoretical curve was calculated for 500 and 13,000 sccm flows, assuming no mass transfer limitation. Recall that $k_{APP}$ is a function of both $k_{KIN}$ and $k_{MT}$ (see equation 4). It can be concluded that any deviation in the actual data from the theoretical kinetically-controlled 13,000 sccm curve can be attributed to the effects of mass transfer. The plateau in conversion at 70% is one such obvious deviation. This analysis is presented graphically in Figure 4.

Using the value for $k_{APP}$ calculated at each temperature using equation (8) for the 13,000 sccm flow, it is possible to generate a plot of $\ln(k_{APP})$ versus 1/T. According to the Arrhenius expression, the resulting curve should be linear, with activation energy being readily obtained from the slope of the curve. The activation energy for surface kinetics is generally of the order 100 to 200 kJ/mol[11], while the activation energy for bulk mass transfer is generally of the order 10 kJ/mol or less. Figure 5 shows the Arrhenius plot of $\ln(k_{APP})$ vs. 1/T for the honeycomb monolith data at 13,000 sccm. Activation energies of 103.3 kJ/mol (T < 250 °C) and 10.3 kJ/mol (T > 280 °C) are calculated for the two regions of the curve. Note that the activation energy for surface kinetics determined from the 13,000 sccm data (103.3 kJ/mol) compares well with that observed previously for the 500 sccm data (107.6 kJ/mol).

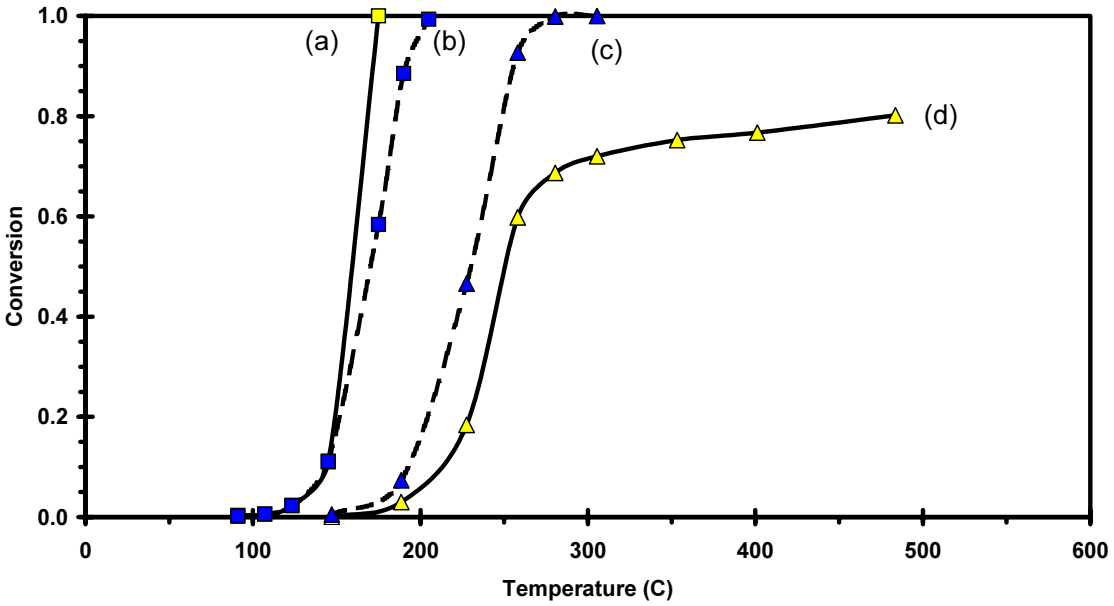


**Figure 4**: Actual data (a) and first order kinetic fit (b) for CO conversion over the honeycomb sample for a 500 sccm flow. The kinetic parameters were used to predict a "theoretical" 13,000 sccm X-T curve (c) for this same sample, assuming no mass transfer limitation. The actual data for a 13,000 sccm flow is shown as curve (d).

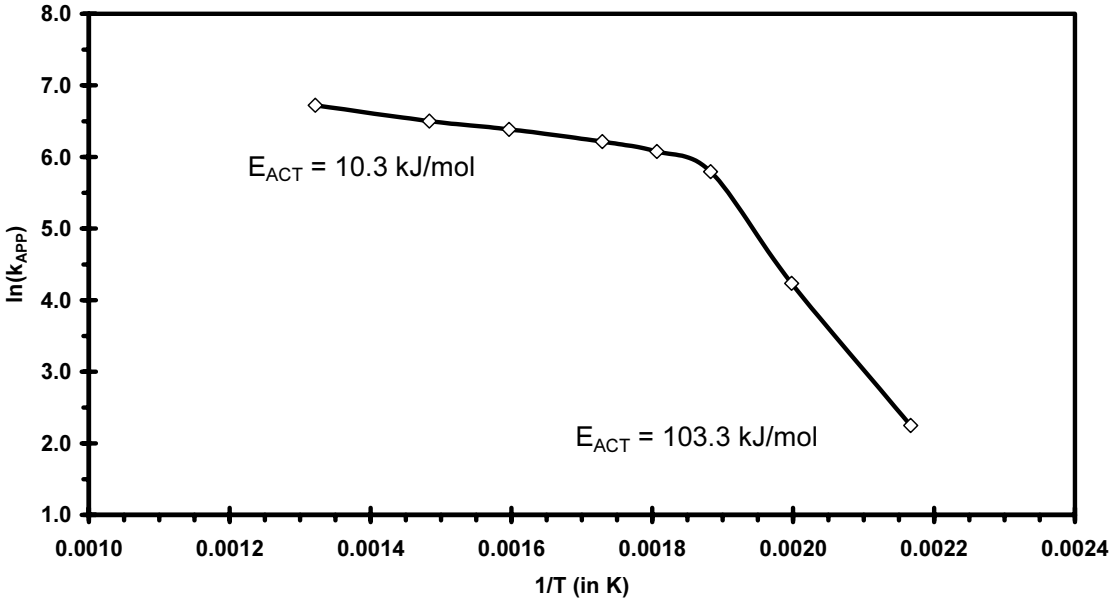


**Figure 5**: Arrhenius plot for the 13,000 sccm honeycomb monolith data.

Finally, the apparent rate constant (for the 13,000 sccm honeycomb data) was plotted versus the temperature (in Kelvin) raised to the 3/2 power. As detailed above in equation (2), diffusion through the boundary layer at the gas-solid interface roughly follows a 3/2 power temperature dependence. Therefore, the linear portion of a plot of $k_{APP}$ vs. $T^{3/2}$ should correspond to bulk mass transfer control. In Figure 6, it can be seen that, for $T^{3/2} > 13{,}000$ (or $T > 280$ °C), the curve is linear, corresponding to diffusion through the boundary layer (i.e. bulk mass transfer control).

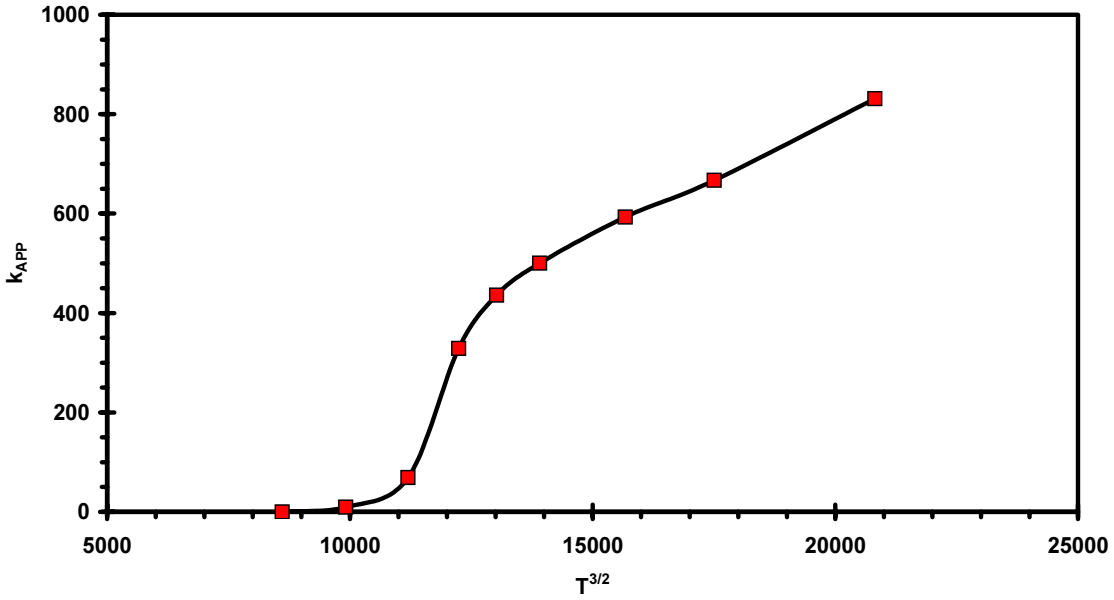


**Figure 6**: Plot of $k_{APP}$ vs. $T^{3/2}$ for the 13,000 sccm honeycomb monolith data.

In section 4.4, it will be shown using the Sherwood number that the experimental results presented in this section detailing the mass transfer limit for honeycomb monoliths are consistent with those found in the literature[12,15,19]. The honeycomb sample will serve as the basis for judging the performance of novel monoliths with alternate geometries.

## 4.2 Robocast Monoliths (FCC and SC)

The "Robo FCC" sample has an FCC-like structure of alternating rods with no line-of-sight pathways. The "Robo SC" monolith is based on a simple cubic (SC) design of rods with line-of-sight pathways. In all other respects, these two samples are identical. Any differences in the performance between the Robo FCC and Robo SC samples can be attributed solely to the difference in placement of the alternating rods that constitute the robocast lattice (i.e. line-of-sight pathways or the lack thereof). The mass transfer efficiency and the pressure drop for these robocast monolith samples can also be compared to the results obtained for the honeycomb sample. Recall that many experimental variables have remained consistent between all samples (see Tables 1 and 2). Therefore, any differences in mass transfer efficiency and pressure drop are attributed solely to differences in sample geometry and porosity.

In the following series of figures, conversion versus temperature is plotted for CO oxidation over the Pt/$\gamma$-$Al_2O_3$-loaded honeycomb and robocast monolith samples. The same data that is shown in Figure 3 is repeated in these figures in order to highlight the similarities and differences in activity between the robocast and honeycomb samples. Figure 7 presents the results for a flow rate of 500 sccm (1% CO in air). This flow rate corresponds to a space velocity (based on overall monolith dimensions) of approximately 30,000 $hr^{-1}$. For each sample, light-off for CO oxidation occurs near 110 ºC, 10% conversion is observed at approximately 140 to 145 ºC, and complete conversion is achieved shortly thereafter. Since there is roughly the same Pt/$\gamma$-$Al_2O_3$ weight loading (and therefore catalytic surface area) in each monolith, the reaction rate (and conversion), when controlled by kinetics, should be nearly identical for each sample. This is exactly what is observed in Figure 7, as each curve is nearly overlapping, within 10 ºC. As concluded previously, a flow rate of 500 sccm is not sufficient to observe mass transfer effects in the three monolith samples studied.

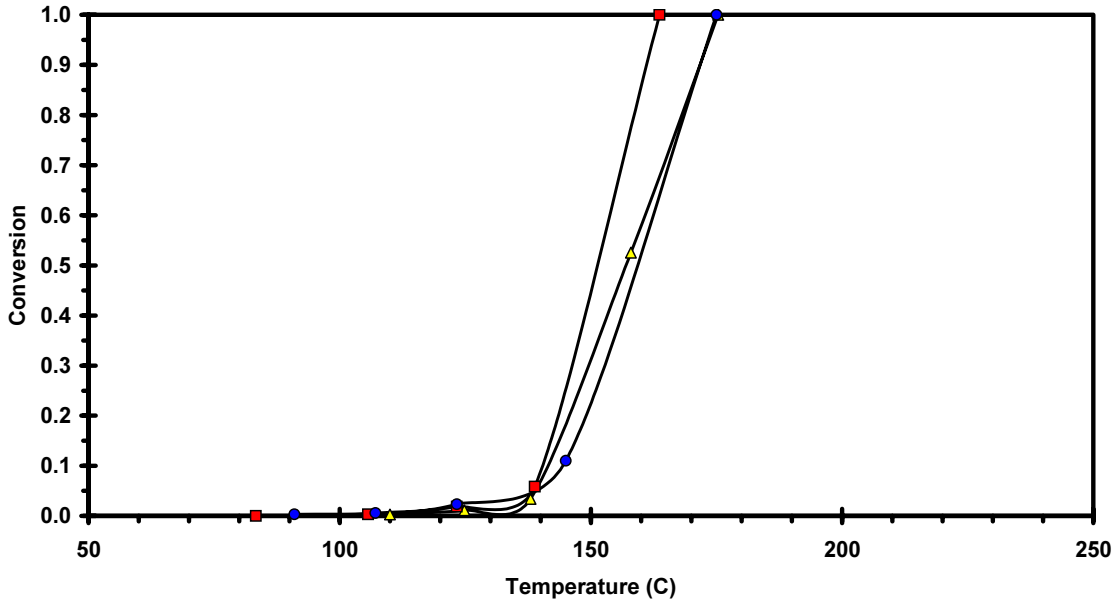


**Figure 7**: CO conversion (500 sccm) over the Robo FCC (□), Robo SC (△), and honeycomb (○)

Figure 8 shows the CO oxidation results for these same monolithic samples (honeycomb, Robo FCC, and Robo SC), again subjected to a flow of 1% CO in air. However, the flow rate has been increased to 10,000 sccm, which is roughly the equivalent of a 575,000 $hr^{-1}$ space velocity. Similar to what is observed in Figure 7, all of the samples basically light off at the same temperature (~170ºC) for a 10,000 sccm flow, and the curves are still nearly identical at 10% conversion. Even at 50% conversion, there is still only a 10 to 15ºC difference from one sample to the next. As detailed previously, surface kinetics controls the reaction rate at these lower temperatures resulting in the similarity between samples (i.e. "overlapping curves").

At higher temperatures differences become apparent that can be attributed to mass transfer. The robocast SC sample exhibits improved mass transfer relative to the honeycomb sample, as evidenced by the higher conversion (~ 90%) for which the "mass transfer plateau" in the X-T data emerges. However, the design of this sample is such that there are still straight-

through channels for fluid flow. The robocast FCC sample is nearly identical in design, except that the rods are alternated such that there are no straight-through channels. This increased tortuosity of the flow pattern should increase the bulk mass transfer rate. This is precisely what can be concluded from Figure 8. There is arguably no mass transfer limit observed for the FCC sample; only at 99% conversion does a slight "tailing" in conversion emerge in the X-T plot.

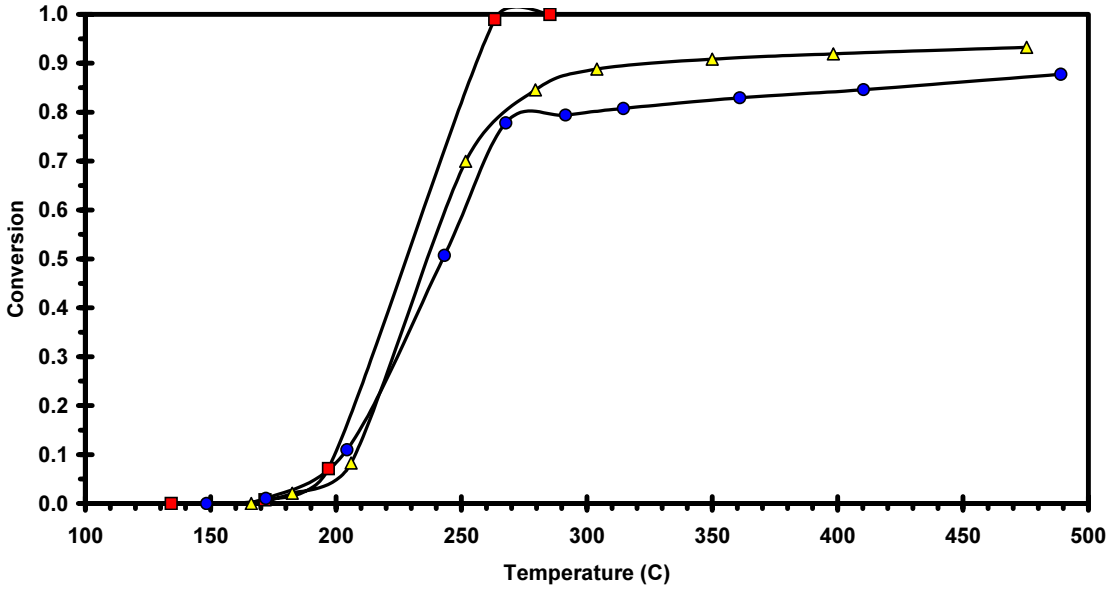


**Figure 8**: CO conversion (10,000 sccm) over the Robo FCC (□), Robo SC (△), and honeycomb (○) samples.

In Figure 9, results are presented (using the same three samples) for a set of CO oxidation experiments run at a flow rate of 13,000 sccm. This flow rate is the equivalent of a space velocity of 750,000 $hr^{-1}$. These results are very similar to those seen in Figure 8, with the biggest difference being that the mass transfer limit for the robocast FCC sample is now fully observable. The general conclusion of mass transfer effectiveness (Robo FCC > Robo SC > honeycomb) is still clearly presented. The mass transfer coefficient for all three samples is calculated and analyzed using the Sherwood number approach in section 4.4 of this report.

The pressure drop across the honeycomb, Robo FCC, and Robo SC samples is presented as a function of space velocity in Figure 10. There is more than an order of magnitude difference in pressure drop between the robocast FCC and SC monoliths and the honeycomb sample. Recall that the bulk porosity of these robocast samples is only 45%, compared to 75% for the honeycomb monolith. This parameter is crucial with respect to pressure drop, and so it is not unexpected that the honeycomb monolith will be superior in this regard. The enhanced mass transfer performance of the robo FCC and robo SC samples does come at a price – in the form of an increased pressure drop. It is interesting that the pressure drop across the Robo SC sample is considerably less than that for the Robo FCC sample, even though the bulk porosity is 45% in each case. Clearly, the tortuous pathway of the Robo FCC sample has a significant effect on the gas flow relative to the straight-through channels of the Robo SC sample.

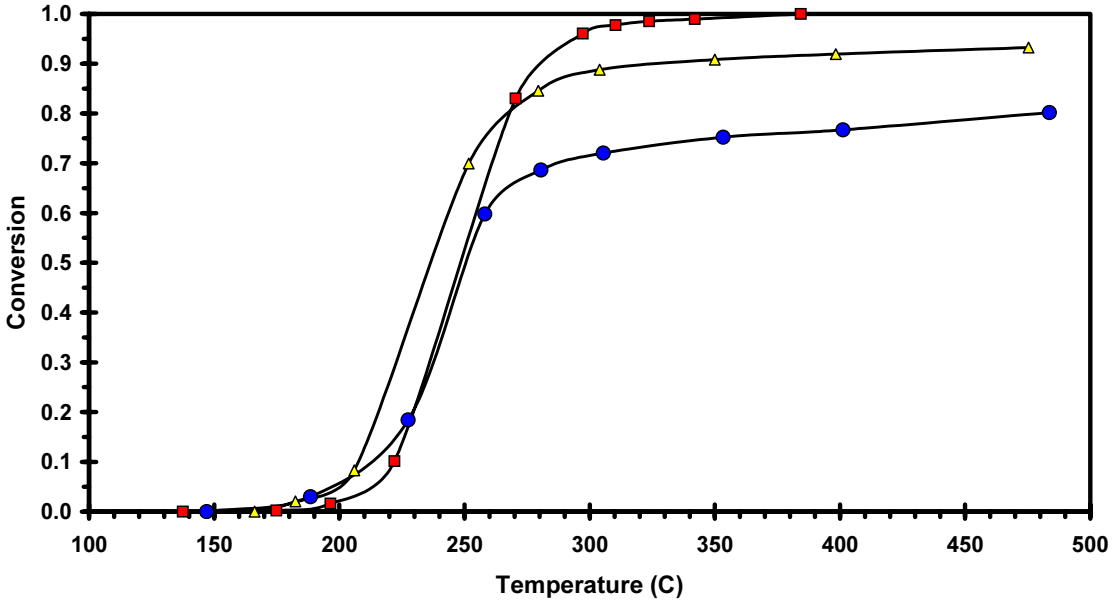


**Figure 9**: CO conversion (13,000 sccm) over the Robo FCC (□), Robo SC (△), and honeycomb (○) samples.

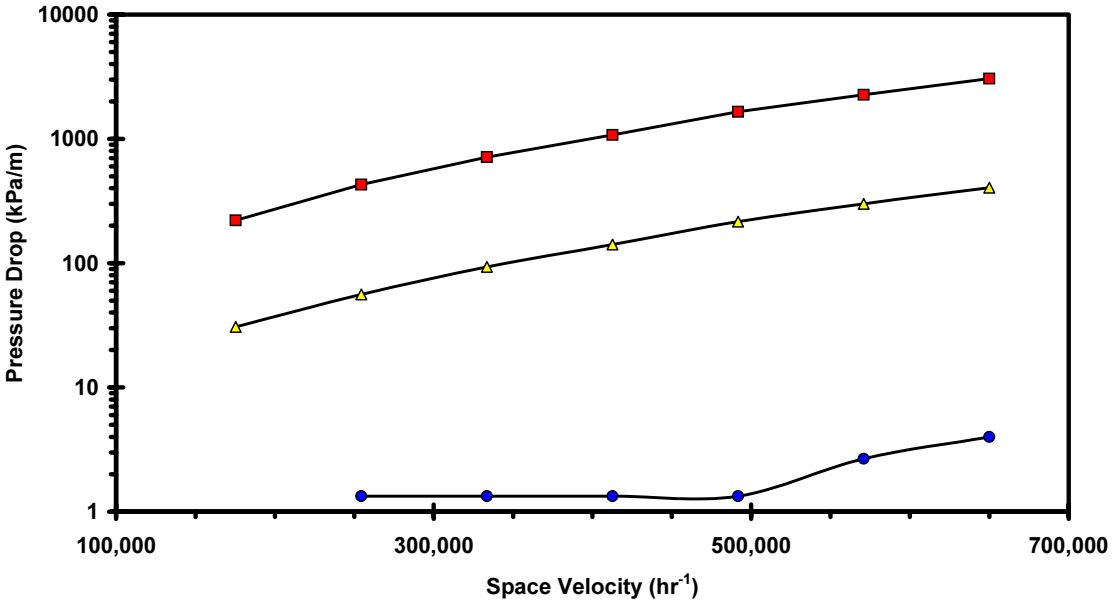


**Figure 10**: Pressure drop across the Robo FCC (□), Robo SC (△), and honeycomb (○) samples.

## 4.3 Robocast Monolith (FCC-74) and Ceramic Foams

The Robo FCC-74 monolith was developed in order to improve upon the pressure drop observed in the previous two robocast samples, while still maintaining enhanced mass transfer relative to the traditional honeycomb monolith. This sample was designed such that the geometric surface area would be remain similar to that of the Robo FCC sample, but the bulk porosity would be significantly improved. The geometric surface area is an important parameter for influencing gas-solid mass transfer, while the bulk porosity is important in determining pressure drop. This improved sample (74% porosity; tortuous pathway for fluid flow with no direct line-of-sight channels) is described in the experimental section. To briefly summarize, an FCC framework is utilized, but every other rod is removed to form a macroscopic "zig-zag" pattern. A smaller rod diameter is employed in order to maintain a comparable geometric surface area.

Ceramic foams are an alternate monolith technology that, like robocast monoliths, can harness the advantages of a tortuous flow path. There are several reports in the literature that detail the synthesis and physical properties of these unique catalyst supports, including the characterization of their pressure drop, mass transfer, and heat transfer properties[5,6,25]. 20 PPI ceramic foam samples were studied to provide an additional point of reference for analyzing the performance of the novel robocast monoliths. The physical properties of the 20 PPI ceramic foam supports are detailed in Table 1. Unfortunately, several key parameters, such as the geometric surface area and bulk porosity, are not close matches with the honeycomb and robocast samples. This provides added complexity (and a distinct advantage to the foam samples) when comparing mass transfer-limited CO conversion data and pressure drop results for the foam, honeycomb, and robocast monoliths studied in this work.

Experimental pressure drop results for the Robo FCC-74 and ceramic foam samples are presented in Figure 11. (For comparison, results for the honeycomb sample are also included.) Relative to the Robo FCC and Robo SC samples (see Figure 10), it can be seen that the Robo FCC-74 sample greatly improves upon the measured pressure drop. For example, at a space velocity of roughly 575,000 $hr^{-1}$, the pressure drop across the Robo FCC and Robo SC samples is approximately 780 and 100 kPa/m, respectively. At this same space velocity, the pressure drop across the Robo FCC-74 monolith is only around 11 kPa/m, a substantial improvement. While this number is still greater than that seen for the honeycomb sample (roughly by a factor of 4), it is at least comparable, and a drastic improvement over what would be expected in a packed bed system. For reference, a packed bed is generally <45% void space, and the pressure drop would be in the realm of that seen for the Robo FCC sample. It is not surprising that the Robo FCC-74 sample exhibits a greater pressure drop than the honeycomb sample, even though the bulk porosities are roughly the same. It is a classic trade-off: a tortuous flow path (with no line-of-sight channels) should increase convective transport phenomena (both mass and heat) while simultaneously increasing pressure drop.

The pressure drop measurements for the ceramic foam sample are nearly identical to those obtained from the Robo FCC-74 monolith. Continuing the previous example, for a space velocity of 575,000 $hr^{-1}$, the pressure drop across the foam support is roughly 10 kPa/m. Considering that both the foam and Robo FCC-74 samples are designed with a tortuous flow path and very porous structure (85% bulk porosity for the foam and 74% for the robocast monolith), it is not surprising that the pressure drop results are so similar. The minor difference in bulk porosity between these two samples likely accounts for the slight difference in pressure

drop. Note that the honeycomb monolith still exhibits the smallest pressure drop of all the tested samples.

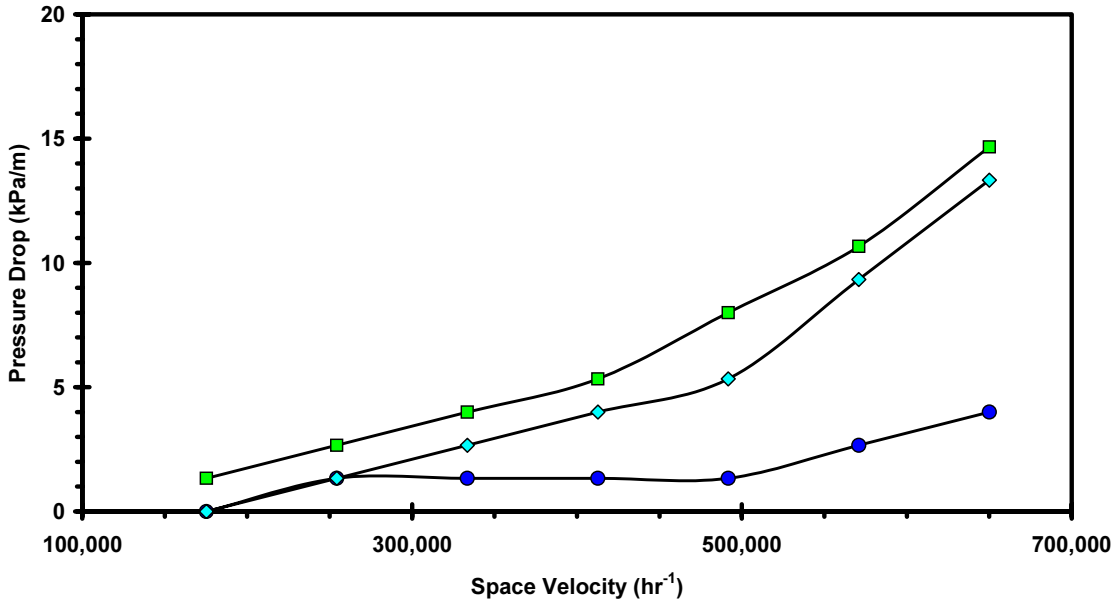


**Figure 11**: Pressure drop across the Robo FCC-74 (□), ceramic foam (◇), and honeycomb (○)

The mass transfer properties of the Robo FCC-74 and ceramic foam samples were tested using the same experimental procedure outlined in the previous sections. X-T results for CO oxidation using flows of 10,000 sccm and 13,000 sccm can be found in Figures 12 and 13. For clarity, the axes have been scaled such that only the mass transfer plateau region of the X-T plot is visible. For comparison, data is also included for the robocast and honeycomb monolith samples detailed in the previous sections. The results presented in Figures 12 and 13 clearly show that the bulk mass transfer efficiency of the new Robo FCC-74 sample exceeds that of the honeycomb monolith. For example, for a flow rate of 13,000 sccm (1% CO in air) at 400 C, both the Robo FCC-74 and honeycomb samples are clearly in the mass transfer-limited regime. Under these conditions, CO conversion for the Robo FCC-74 sample is 84%, compared to only 76% for the honeycomb sample. While the Robo FCC-74 monolith clearly outperforms the honeycomb monolith, it is evident that the robocast FCC sample is still superior with respect to mass transfer.

As observed for the robocast samples, the 3-dimensional structure of the ceramic foam support enhances the mass transfer rate relative to that of the straight-channeled honeycomb monolith. The 20 PPI foam even exhibits slightly greater conversions (2 to 3%) than the Robo FCC-74 sample. However, recall that the foam sample actually possesses roughly 50% more extrinsic surface area than does the porous robocast sample. Since the geometric surface area is proportional to the rate for gas-solid mass transfer, it is likely that the conversion measured at a given flow rate for a new robocast sample with smaller rods (and matching surface area) would be identical to, or even exceed the CO conversion obtained from the foam sample. Regardless, it can be concluded that the ceramic foam (20 PPI) and Robo FCC-74 supports are quite similar

with respect to bulk mass transfer efficiency, and both supports represent a good compromise between enhanced mass transfer (relative to the honeycomb support) and pressure drop.

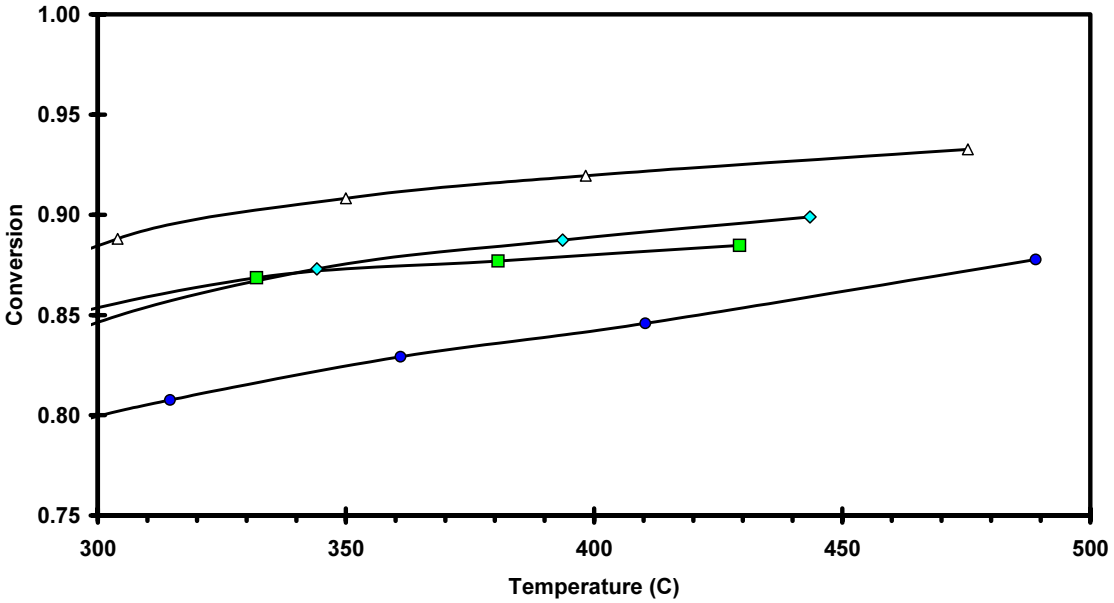


**Figure 12**: CO conversion (10,000 sccm) over the Robo SC (△), ceramic foam (◇), Robo FCC-74 (□) and honeycomb (○) samples.

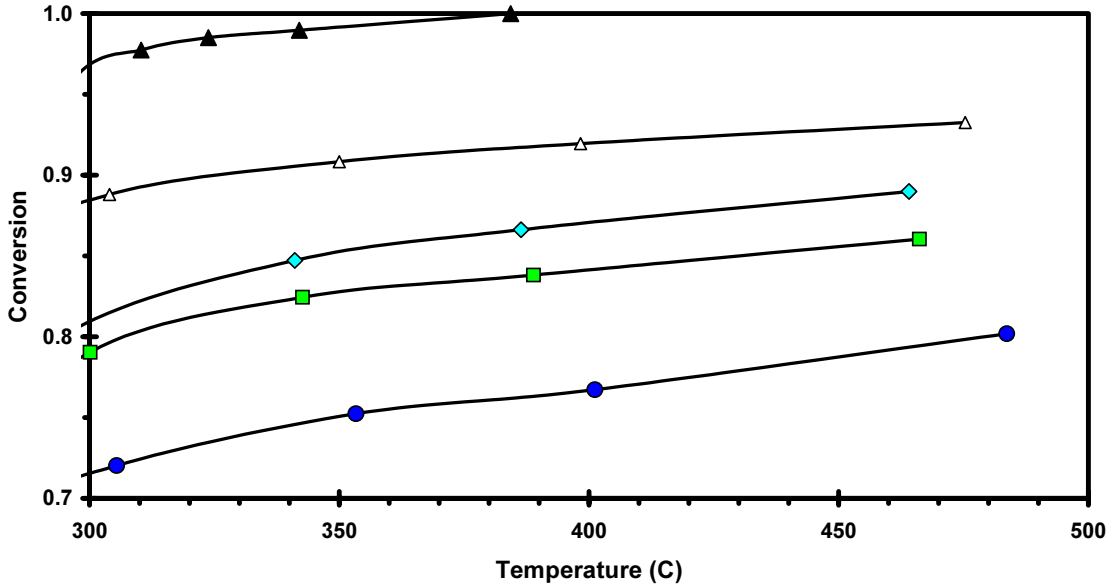


**Figure 13**: CO conversion (13,000 sccm) over the Robo FCC (▲), Robo SC (△), ceramic foam (◇), Robo FCC-74 (□) and honeycomb (○) samples.

## 4.4 Quantitative Analysis – Sherwood Number

To quantify the trends in gas-solid mass transfer presented above, the Sherwood number for each monolith sample was determined as a function of the Graetz number. This was done using the following procedure. First, $k_{KIN}(T)$ was derived from the kinetically-limited 500 sccm data. This result was then used (in conjunction with equations 3 and 7) to obtain $k_{MT}(T)$ from the mass-transfer-limited X-T data for the two highest flow rates (10,000 sccm and 13,000 sccm). Using this value for $k_{MT}$, the Sherwood number was then calculated for each mass transfer-limited data point. The Graetz number ($N_{GZ} = N_{RE}*(d_H/L)*N_{SC}$) was also calculated for these same data points. Finally, a plot of Sherwood versus Graetz numbers (for each sample) was generated. The results from this analysis are presented in Figure 14, along with the three empirical curves[12,15,19] detailed previously (equations 12, 16, and 17) for mass transfer in straight-channel monoliths. This quantitative analysis ($N_{SH}$ vs. $N_{GZ}$) is a useful method for directly comparing the structural impact on bulk mass transfer for different monolith samples, as all important system parameters are included in the calculations, and differences in surface area, porosity, etc, are, in effect, "normalized" out.

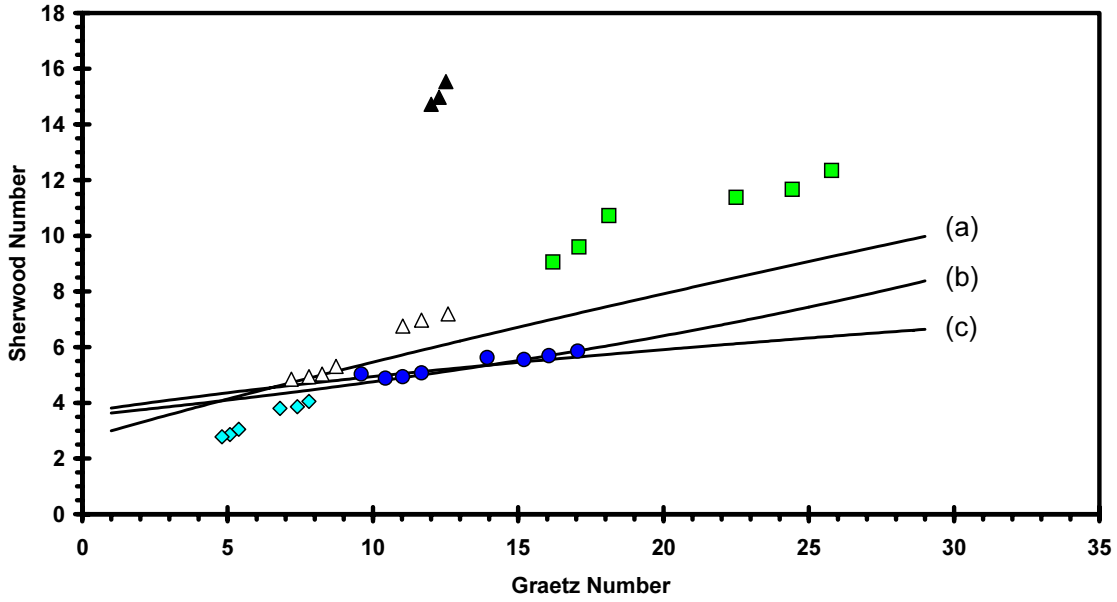


**Figure 14**: $N_{SH}$ vs. $N_{GZ}$ for all samples: Robo FCC (▲), Robo SC (△), ceramic foam (◇), Robo FCC-74 (□) and honeycomb (○). Also shown are the empirical correlations for straight-channel monoliths generated by (a) Uberoi and Pereira, (b) Holmgren and Andersson, and (c) Hawthorn.

The first thing to note is that the data points generated from the experimental honeycomb data presented in this work are completely consistent with the empirical correlations for straight-channel monoliths (particularly those developed by Holmgren and Anderson, and Hawthorn). This result is encouraging, as it provides strong evidence for the validity of the experimental results and data analysis presented in this work. Figure 14 clearly shows that the Robo FCC sample is, by far, the best monolith studied for minimizing the negative effects of bulk mass

transfer. For a given $N_{GZ}$, there is nearly a factor of three increase in $N_{SH}$ for the Robo FCC sample relative to the honeycomb data and correlations. Recall that $N_{SH}$ is directly proportional to the rate of convective mass transfer. Only $N_{SH}$ vs. $N_{GZ}$ data for the 13,000 sccm flow is presented for the Robo FCC sample in Figure 14, as it was unclear that mass transfer was even a factor for the 10,000 sccm CO oxidation data. As expected, the Sherwood number (for a given $N_{GZ}$) for the Robo SC and Robo FCC-74 samples are both greater than what is predicted from the empirical correlations for straight-channel monoliths, proving that these robocast samples do indeed enhance mass transfer. Note that the $N_{SH}$ for all robocast and honeycomb monolith samples (including the literature correlations) tends to converge to a value between 3 and 4 as $N_{GZ}$ approaches zero. Due to the larger porosity and geometric surface area values for the 20 PPI ceramic foam, the $N_{SH}$ vs. $N_{GZ}$ data points for this sample fall within this region of convergence. Therefore, it is difficult to draw any conclusions regarding mass transfer for the foam's "sponge-like" geometry relative to the periodic lattice of the robocast samples and the adjoining, straight-through channels of the honeycomb sample. Unfortunately, the flow reactor system is currently unable to achieve the higher flow rates necessary to probe the ceramic foam sample at larger $N_{GZ}$ values. It is a bit troubling that the foam data points actually seem to fall below the empirical correlation lines. This is likely due to either a breakdown in the correlations for small $N_{GZ}$, or the uncertainty in foam's geometric parameters used for the quantitative analysis.

### 4.5 Quantitative Analysis - $J_D$ factor

The $J_D$ factor is an alternate method for quantifying mass transfer. Recall that $J_D$ is a function of $N_{SH}$, so it is expected that similar conclusions regarding mass transfer efficiency will be drawn from the analysis that follows. Using equation (20), $J_D$ was simply calculated from the dimensionless numbers generated during the quantitative analysis presented in section 4.4. Recall that many empirical expressions have been developed relating $J_D$ to the Reynolds number. The following commonly used correlation, published by Dwivedi and Upadhyay[28], describes gas flow through a packed bed of spheres:

$$\varepsilon \times J_D = 0.455\ N_{RE}^{-0.407} \qquad (23)$$

Richardson, et al.[6] have developed the following similar correlation for gas flow in a 30 PPI ceramic foam:

$$\varepsilon \times J_D = 0.233\ N_{RE}^{-0.416} \qquad (24)$$

Plotted in Figure 15 are these two empirical correlations (equations 23 and 24), as well as the $\varepsilon J_D$ vs. $N_{RE}$ data points generated from the experimental results for all the samples presented in this work. Greater values of $\varepsilon J_D$ for a given $N_{RE}$ equate to a faster bulk mass transfer.

In Figure 15, it is observed that the data points for the 20 PPI ceramic foam sample studied in this work are in close agreement with the empirical curve for ceramic foams reported by Richardson, et al. The fact that the experimentally determined $\varepsilon J_D$ values for this sample are actually slightly less than that predicted by the empirical correlation is not surprising, as the 20 PPI foams studied in this work are likely to have a slightly less tortuous flow pattern than the 30 PPI foams from which the empirical correlation was derived. Once again, this consistency

between experiment and empirical correlation for the same support provides strong evidence of the validity of the experimental results and mass transfer calculations presented in this study.

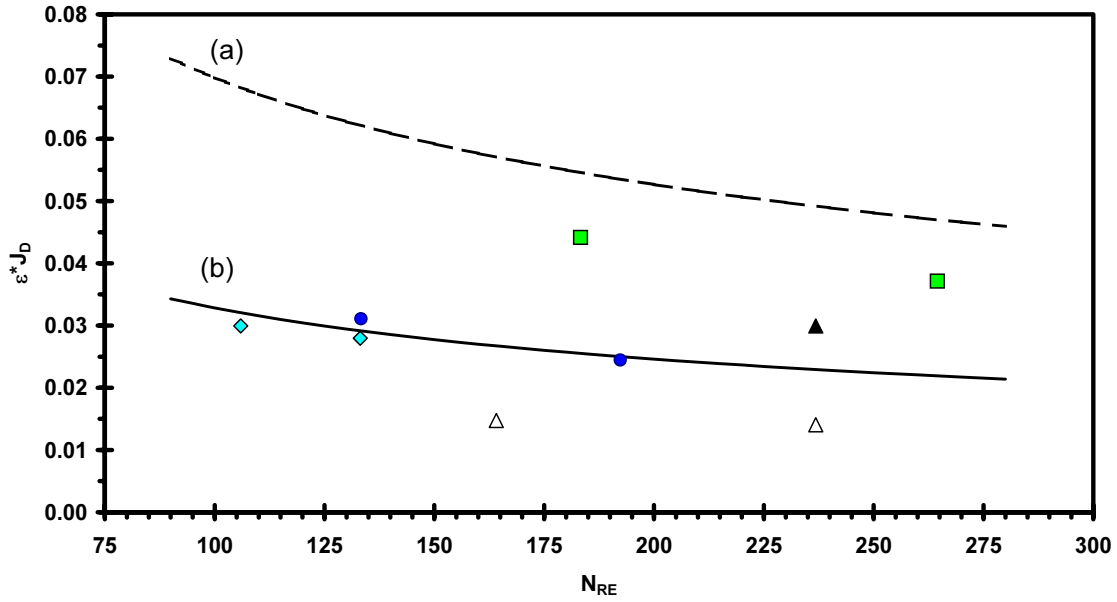


**Figure 15**: $\varepsilon J_D$ vs. $N_{RE}$ for all samples: Robo FCC (▲), Robo SC (△), ceramic foam (◇), Robo FCC-74 (□) and honeycomb (○). Also shown are the empirical correlations for (a) packed beds by Dwivedi and Upadhyay, and (b) 30 PPI ceramic foams by Richardson, et al.

The plot of $\varepsilon J_D$ vs. $N_{RE}$ (Figure 15) provides additional insights into the experimentally obtained CO oxidation results. In Figure 14, the plot of $N_{SH}$ vs. $N_{GZ}$ shows the Robo FCC sample to be best with respect the rate of mass transfer. In Figure 15, the sample that best approaches the "ideal" bulk mass transfer efficiency of a packed bed of spheres is the Robo FCC-74 monolith. This result seems counter-intuitive in light of the fact that the Robo FCC sample demonstrated the greatest mass transfer-limited CO conversion. However, the result is understandable since bulk porosity is an important system parameter for the $\varepsilon J_D$ vs. $N_{RE}$ analysis, and the bulk porosities of the two FCC-like robocast samples is significantly different. When comparing samples of similar porosity (Robo FCC-74, honeycomb, and ceramic foam), it is clear that the geometry of the Robo FCC-74 sample is most efficient at enhancing mass transfer. From Figure 15 it can be approximated that $\varepsilon J_D$ for the Robo FCC-74 sample (for a given $N_{RE}$) is nearly twice that of the honeycomb and foam samples. It is somewhat surprising that the honeycomb and foam samples appear almost identical with respect to mass transfer when plotted as $\varepsilon J_D$ vs. $N_{RE}$. Since this analysis accounts for geometric surface area, Figure 15 seems to suggest that the improved CO oxidation activity (i.e. mass transfer limit) of the ceramic foam sample relative to the honeycomb sample results solely from the increased extrinsic surface area, rather than from a tortuous flow path that enhances mass transfer. This sort of speculation can best be resolved in future studies that utilize ceramic foam supports that more closely match the important geometric properties of the honeycomb and robocast samples to be studied.

## 4.6 Additional Comments

This work focused on two important reactor design parameters: bulk mass transfer, and pressure drop. It is worth bearing in mind that there are other parameters that one must consider when comparing the various available options. It is expected that the tortuous pathway of the robocast sample will serve to enhance convective heat transfer. While no direct experimental evidence has yet been obtained, computer simulations suggest that radial heat transfer is enhanced in the periodic lattice structure of the robocast monolith. Likewise, engineering texts often highlight the many fundamental similarities in the correlations for quantifying mass and heat transfer. For example, the widely used Chilton Colburn analogy[18] is as follows:

$$J_H = (h / C_P \times G) \times N_{SC}^{2/3} = J_D = (k_{MT}/\nu) \times NSC^{2/3} \qquad (25)$$

Therefore, it is reasonable to assume that geometric factors that increase bulk mass transfer will also enhance convective heat transfer as well. This result holds promising implications, as "hot spots" that lead to catalyst deactivation (through sintering or even evaporation), particularly in the harsh environment of a catalytic combustor, are likely to be minimized in a robocast monolith. Perhaps even more importantly, the use of monolith reactors for heat transfer limited reactions, such as steam reforming, can be explored.

Mechanical integrity is another important consideration in determining which monolith reactor (if any) is suitable for a particular application. This is one of the inherent strengths of the robocasting process, as there is a great deal of intimate contact (and mechanical strength) between the rods that compose the robocast lattice, and this will result in greater durability over the lifetime of the monolithic reactor. Also, due to the precision and nature of the robocasting apparatus, weak points in the monolith are minimized for a repeating lattice of alternating rods. This is not true for synthesis of ceramic foams, which basically consist of a series of interlocking and random pores.

Flexibility of synthetic materials of construction is an important processing advantage for robocast monoliths. It is possible to construct a robocast monolith, once the relevant slurry processing parameters are determined, from many different materials, including catalysts such as BaMn-hexaaluminates. In fact, one such monolith has already been synthesized, and the results for methane catalytic combustion are very promising[29].

Finally, another important advantage of robocast monoliths is the customization of geometry. This variable is essentially limited by the creativity of the designer, as software is in place to robocast virtually any CAD image to an actual ceramic part. The results for the three different robocast samples presented in this work suggest that an optimal monolith can be developed, depending on the needs of the particular application. By adjusting design parameters (primarily rod size, arrangement, and spacing) the bulk porosity, extrinsic surface area, and monolith geometry can all be adjusted and tuned to provide the optimum trade-off between conversion (assuming operation in the mass or heat transfer limited regime) and pressure drop.

# 5. Conclusions

Monolith reactors are increasingly being studied for a wide range of catalytic applications, with catalytic combustion of natural gas for clean energy production being a prime candidate. In this report, a traditional honeycomb monolith support (400 cpsi) is characterized for its mass transfer efficiency and pressure drop. These results, consistent with those found in the literature, are then used as a basis for evaluating novel monolith designs with periodic, 3-D geometries aimed at enhancing the rate of bulk mass transfer. These unique monolith supports, synthesized using the robocasting process, are shown to possess superior bulk mass transfer rates relative to the honeycomb monolith. The robocast FCC monolith, consisting of offset rods in alternating directions with no direct line-of-sight pathways for fluid flow, exhibits the greatest mass transfer efficiency (i.e. the highest mass transfer-limited CO conversion and Sherwood numbers), but also results in the greatest pressure drop. The robocast FCC-74 monolith, with a "modified FCC" structure, provides enhanced mass transfer compared to the honeycomb sample, with only a relatively small pressure drop penalty. Finally, the mass transfer-limited CO conversion and pressure drop for a ceramic foams support (20 PPI) closely resembles those for the robocast FCC-74 sample. However, quantification via the Sherwood number and $J_D$ factor both suggest that the robocast FCC-74 sample is more efficient at bulk mass transfer.

## References


1. Heck, R. M., Gulati, S., Farrauto, R.J. The application of monoliths for gas phase catalytic reactions. *Chemical Engineering Journal* **82**, 149-156 (2001).
2. Williams, J. L. Monolith structures, materials, properties and uses. *Catalysis Today* **69**, 3-9 (2001).
3. Geus, J. W., van Giezen, J.C. Monoliths in catalytic oxidation. *Catalysis Today* **47**, 169-180 (1999).
4. Thevenin, P. O., Menon, P.G., Jaras, S.V. Catalytic total oxidation of methane. *CatTech* **7**, 10-22 (2003).
5. Richardson, J. T., Peng, Y., Remue, D. Properties of ceramic foam catalyst supports: pressure drop. *Applied Catalysis A: General* **204**, 19-32 (2000).
6. Richardson, J. T., Remue, D., Hung, J.-K. Properties of ceramic foam catalyst supports: mass and heat transfer. *Applied Catalysis A: General* **250**, 319-329 (2003).
7. McCarty, J. G. Durable catalysts for cleaner air. *Nature* **403**, 35-36 (2000).
8. Dalla Betta, R. A. Catalytic combustion gas turbine systems: the preferred technology for low emissions electric power production and co-generation. *Catalysis Today* **35**, 129-135 (1997).
9. Groppi, G., Cristiani, C., Forzatti, P. Preparation, characterisation and catalytic activity of pure and substituted La-hexaaluminate systems for high temperature catalytic combustion. **35**, 137-148 (2001).
10. Choudhary, T. V., Banerjee, S., Choudhary, V.R. Catalysts for combustion of methane and lower alkanes. *Applied Catalysis A: General* **234**, 1-23 (2002).
11. Heck, R. M., Farrauto, R.J. *Catalytic Air Pollution Control* (Van Nostrand Reinhold, New York, NY, 1995).
12. Uberoi, M., Pereira, C.J. External Mass Transfer Coefficients for Monolith Catalysts. *Industrial & Engineering Chemistry Research* **35**, 113-116 (1996).
13. Duprat, F. Light-off curve of catalytic reaction and kinetics. *Chemical Engineering Science* **57**, 901-911 (2002).
14. Hayes, R. E., Kolaczkowski, S.T. A study of Nusselt and Sherwood numbers in a monolith reactor. *Catalysis Today* **47**, 295-303 (1999).
15. Holmgren, A., Andersson, B. Mass transfer in monolith catalysts - CO oxidation experiments and simulations. *Chemical Engineering Science* **53**, 2285-2298 (1998).
16. Thiel, P. A., Williams, E.D., Yates, Y.T., Weinberg, W.H. Chemisorption of CO on Rh(111). *Surface Science* **84**, 54-64 (1979).
17. Root, T. W., Schmidt, L.D. Nitric Oxide Reduction by CO on Rh(111): Temperature Programmed Reaction. *Surface Science* **150**, 173-192 (1985).
18. Geankoplis, C. J. *Transport Processes and Unit Operations* (Prentice Hall, Englewood Cliffs, New Jersey, 1993).
19. Hawthorn, R. D. Afterburner catalysts - effects of heat and mass transfer between gas and catalyst surface. *A.I.Ch.E. Symp. Ser.* **70**, 428-438 (1974).
20. Vortruba, J., Mikus, O., Nguen, K., Hlavacek, V., Skrivanek, J. Heat and mass transfer in honeycomb catalysts - II. *Chemical Engineering Science* **30**, 201-206 (1975).
21. Holmgren, A. M. Enhanced Mass Transfer in Monolith Catalysts with Bumps on the Channel Walls. *Industrial & Engineering Chemistry Research* **38**, 2091-2097 (1999).

22. Bird, R. B., Stewart, W.E., Lightfoot, E.N. *Transport Phenomena* (John Wiley & Sons, New York, NY, 1960).
23. Fuller, E. N., Schettler, P.D., Giddings, J.C. A New Method for the Prediction of Gas-Phase Diffusion Coefficients. *Industrial & Engineering Chemistry Research* **58**, 19-27 (1966).
24. Hayes, R. E., Kolaczkowski, S.T. Mass and Heat Transfer Effects in Catalytic Monolith Reactors. *Chemical Engineering Science* **49**, 3587-3599 (1994).
25. Twigg, M. V., Richardson, J.T. *Preparation and properties of ceramic foam catalyst supports* (ed. al., G. P. e.) (Elsevier Science, 1995).
26. Weast, R. C., Astle, M.J., Beyer, W.H. *CRC Handbook of Chemistry and Physics, 64th Edition* (ed. 1974) (CRC Press, Inc., Boca Raton, FL, 1974).
27. Satterfield, C. N. *Mass Transfer in Heterogeneous Catalysis* (MIT Press, Cambridge, MA, 1970).
28. Dwivedi, P. N., Upadhyay, S.N. *Ind. Eng. Chem., Proc. Res. Dev. Eng. Sci.* **16**, 157 (1977).
29. Stuecker, J. N., Miller, J.E., Ferrizz, R.M., Mudd, J.E., Cesarano III, J. Advanced Support Structures for Enhanced Catalytic Activity. *Industrial & Engineering Chemistry Research*, in press.
30. Stuecker, J. N., Cesarano III, J., Hirschfeld, D.A. Control of the Viscous Behavior of Highly Concentrated Mullite Suspensions For Robocasting. *Journal of Materials Processing Technology* **142**, 318-325 (2003).
31. Cesarano III, J., Calvert, P.D. Patent #6,027,326 (USA, 1997).
32. Cesarano III, J., Segalman, R., Calvert, P. Robocasting Provides Moldless Fabrication from Slurry Deposition. *Ceramic Industry* **148**, 94-102 (1998).
33. Torncrona, A., Skoglundh, M., Thormahlen, P., Fridell, E., Jobson, E. Low temperature catalytic activity of cobalt oxide and ceria promoted Pt and Pd: - influence of pretreatment and gas composition. *Applied Catalysis B: Environmental* **14**, 131-146 (1997).
34. Kolaczkowski, S. T. Modeling catalytic combustion in monolith reactors - challenges faced. *Catalysis Today* **47**, 209-218 (1999).

**DISTRIBUTION:**

| | | |
|---|---|---|
| 5 | MS 0867 | Robert Ferrizz, 14405 |
| 5 | MS 1349 | Jim Miller, 1846 |
| 5 | MS 1349 | Joseph Cesarano, 1843 |
| 2 | MS 1349 | John Stuecker, 1843 |
| 1 | MS 0887 | Michael Cieslak, 1800 |
| 1 | MS 1411 | Jun Liu, 1846 |
| 1 | MS 1349 | William Hammetter, 1843 |
| 1 | MS 0867 | Larry Pope, 6233 |
| 1 | MS 1349 | Lindsey Evans, 1846 |
| 1 | MS 1349 | Ronald Sandoval, 1846 |
| 1 | MS 0741 | Marjorie Tatro, 6200 |
| 1 | MS 0741 | Rush Robinett, 6200 |
| 1 | MS 9054 | Donald Hardesty, 8360 |
| 1 | MS 9053 | Jay Keller, 8367 |
| 1 | MS 0734 | Bruce Kelley, 6245 |
| 1 | MS 0701 | John Merson, 6102 |
| 1 | MS 0885 | Grant Heffelfinger, 1802 |
| 1 | MS 1349 | Michael Prairie, 9112 |
| | | |
| 1 | MS 9018 | Central Technical Files, 8945-1 |
| 2 | MS 0899 | Technical Library, 9616 |